RockNet: Rockfall and earthquake detection and association via multitask learning and transfer learning

Wu-Yu Liao , En-Jui Lee , Chung-Ching Wang, Po Chen , Floriane Provost , Clément Hibert , and Jean-Philippe Malet , Chung-Ray Chu, and Guan-Wei Lin

***Abstract*—Seismological data can provide timely information for slope failure hazard assessments, among which rockfall waveform identification is challenging for its high waveform variations across different events and stations. A rockfall waveform does not have typical body waves as earthquakes do, so researchers have made enormous efforts to explore characteristic function parameters for automatic rockfall waveform detection. With recent advances in deep learning, algorithms can learn to automatically map the input data to target functions. We develop RockNet via multitask and transfer learning; the network consists of a single-station detection model and an association model. The former discriminates rockfall and earthquake waveforms. The latter determines the local occurrences of rockfall and earthquake events by assembling the single-station detection model representations with multiple station recordings. RockNet achieves macro F1 scores of 0.990 and 0.981 in terms of discriminating earthquakes and rockfalls from other events with the single-station detection and association models, respectively.**

***Index Terms*—multitask learning, transfer learning, rockfall seismic monitoring.**

I. Introduction

ROCKFALL is one of the socioeconomic exposure risks in mountainous areas that correlates with other slope failures (e.g., landslides and debris flow). Rockfall studies usually consider meteorological factors [1]–[4] and geomorphological evolution via instruments like airborne LiDAR and terrestrial laser scanning (TLS) that generates high-resolution topographic data [5]–[9]. Time-lapse imaging of rockfalls obtained from stereographic pairs of sequential photographs and cameras is also intuitive for rockfalls identification [4], [10]. Although these methods have facilitated rockfall studies in various aspects, none are almighty and exist deficiencies. LiDAR and TLS are expensive when applied to vast areas and are ineffective during heavy rains that cause much light refraction. Photo monitoring is susceptible to environmental visibility, such as foggy and rainy weather, and poor performance at night. Seismogram recorded by seismometers is emerging as regular monitoring data for providing timely dynamic process of mass movements. Seismic monitoring is relatively cost-effective and free from weather impacts compared to other methods. Furthermore, the seismological analysis conducted in the time and time-frequency domains could provide physical parameters like source-receiver distance, magnitude, and source location [11]–[13]; in which the seismic energy attenuates with distances and is correlated with rockfall volume and mechanisms.

The challenge of rockfall seismic monitoring is identifying rockfall-induced signals on continuous seismic recordings. A general technique to achieve automatic rockfall waveform detection is to apply an amplitude-sensitive algorithm in the time or frequency domain to find potential events and confirm these events based on a self-designed criterion [2]. Advanced methods depend on machine learning algorithms and self-defined seismic attributes to distinguish various seismic sources [14], [15]. However, rockfall waveforms differ according to the source mechanisms coupled with their propagation media, numbers of blocks, volumes, and movements, causing generalization problems of the detection algorithm [11], [16]–[18]. In this study, we train a deep-learning model that automatically extracts features from the input waveforms and the spectrograms of all stations in the seismic network, which can further gain model generalizability by including waveforms of various source mechanisms.

Figure 1 provides an overview of this study. We collected and labeled four types of seismic events recorded by a local seismic network, with a station spacing of less than 1 km, and deployed them near a slope failure site. The geometry of the deployed seismic network could impose physical constraints on seismic event confirmation according to the physics of the observed signals. For example, due to the short spacing, an earthquake waveform's appearance and arrival time would be coherent across the stations. In contrast, the arrival of a rockfall waveform would have little time delay among all stations, and the ground motion recordings would become increasingly unclear as the wave propagation distance increased. Therefore, one could confirm a local seismic network's rockfall and earthquake events by associating the interpretation results of all single-station recordings. Following this logic, we develop RockNet, which consists of two models. A single-station detection model learns to identify earthquake and rockfall

W. Liao, E. Lee, C. Wang, and G. Lin are with Department of Earth Science, National Cheng-Kung University, Taiwan

P. Chen is with Department of Geology and Geophysics, University of Wyoming, Laramie, Wyoming, U.S.A.

F. Provost, C. Hibert, and J.-P. Malet are with Institut Terre et Environnement de Strasbourg (ITES), CNRS UMR 7063 - Université de Strasbourg, 5 rue Descartes, F-67084 Strasbourg, France

C. Hibert, and J.-P. Malet are with Ecole et Observatoire des Sciences de la Terre (EOST-OMIV), CNRS UAR830, Université de Strasbourg, 5 rue Descartes, F-67000 Strasbourg, France

C. C is with the National Science and Technology Center for Disaster Reduction

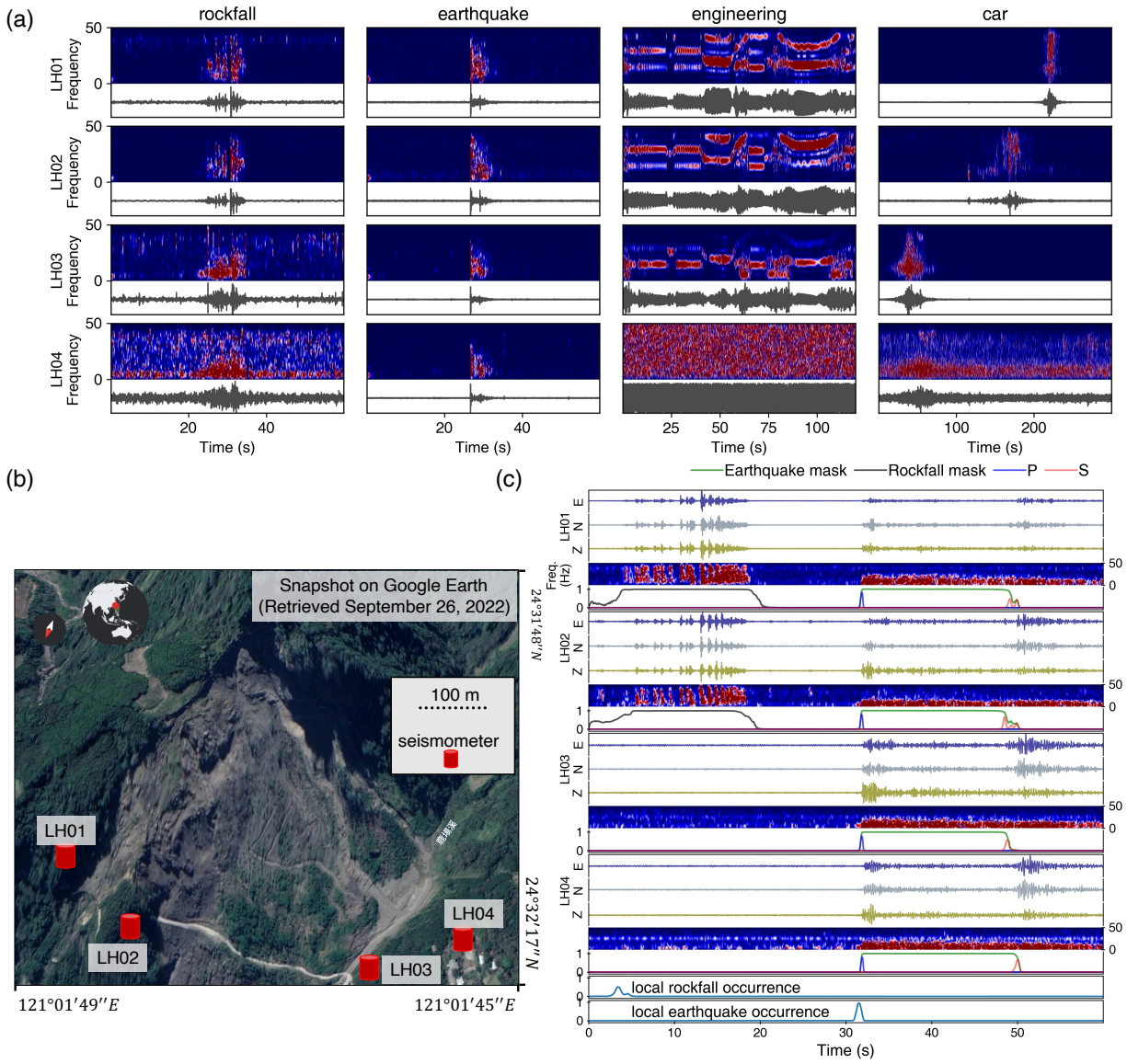

Fig. 1. Overview of the collected seismic signals and the model outputs. (a) Seismic signals recorded over the local network: rockfalls, earthquakes, engineering signals, and car-induced vibrations. For simplicity, we only plot the vertical-component data. The missing data are substituted with random values. (b) Local seismic network geometry. (c) A detection example including rockfall and earthquake events recorded at close time points. For each station, the single-station detection model generates earthquake P and S phase-time functions (blue and red lines, respectively), earthquake waveform masking functions (green lines), and rockfall waveform masking functions (black lines). The association model aggregates the encoded features of all station recordings from the single-station detection model and generates the local occurrence time functions of rockfall and earthquake events. The model inputs are three-component waveforms and the vertical-component spectrograms of all stations.

waveforms on single-station recordings. An association model assigns the local occurrence times of earthquake and rockfall events based on the waveform interpretations made by the single-station detection model.

II. Data

From 2019/02/26 to 2020/12/31, we deployed a local seismic network with four three-component-geophone produced by DiGOS sampled at 100 Hz in the Luhu tribe, Miaoli, Taiwan, where rockfall events have been frequent since a slope failure event occurred in April 2018 (Figure 1 (b)). The main traffic artery of the monitoring site was closed due to the presence of unstable slopes. We assumed that the main seismic events in this area were earthquakes, rockfalls, slope stabilization engineering events, and car-induced vibrations (Figure 1 (a)). In this study, we include additional datasets to develop our models: the Taiwan earthquake dataset and the STEAD dataset [19] for the single-station detection model, the INSTANCE dataset [20] for the association model, and the artificial rockfall experiment waveforms [18] for both models. We further apply data augmentation and oversampling strategies to alleviate imbalanced data issues during model training.

A. Luhu dataset

To compile the database from almost two years of continuous recordings, we applied STA/LTA algorithms [21] to detect pulse-

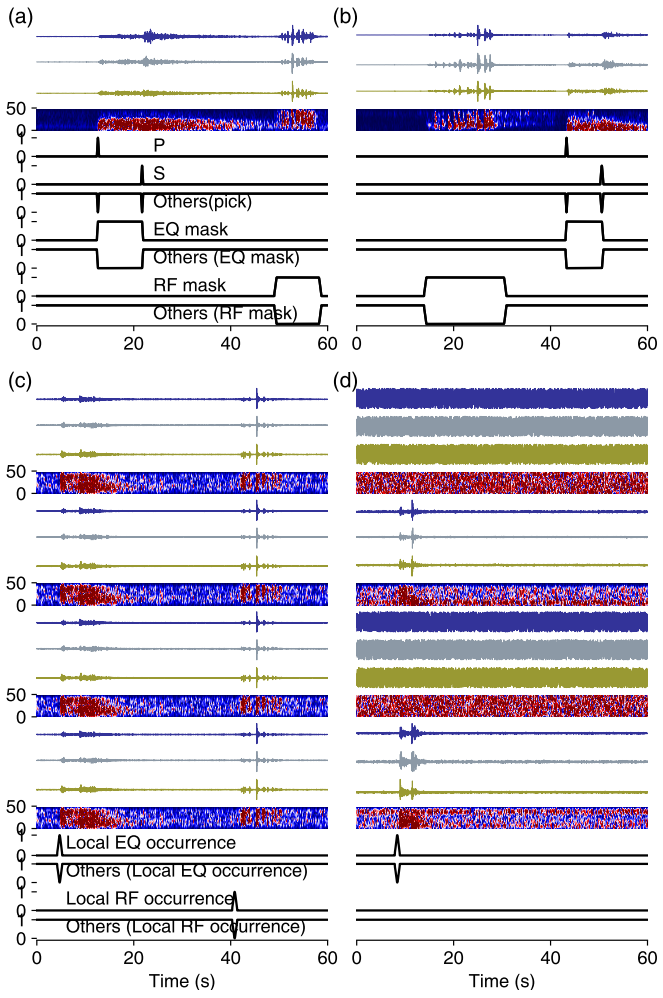

Fig. 2. Templates of the model input waveforms and corresponding target functions for (a)(b) the single-station detection model and (c)(d) the association model. RF and EQ are abbreviations of rockfall and earthquake events, respectively. We transform the time labels (i.e., the P and S arrival times and the local occurrences of earthquake and rockfall waveforms) into truncated Gaussian functions. (a)(b) Marching mosaic waveforms are generated by randomly superimposing the earthquake and rockfall waveforms and shifting them back and forth. (c) The earthquake-rockfall mosaic waveforms generated for the single-station detection model are replicated four times as the augmentation data for the association model. (d) An earthquake event from the Luhu dataset with a random station order. We replace the waveform data with random values for the stations with missing data or ground-truth labels.

like signals and then manually labeled the events according to our experiences of encountered rockfalls during field works. Unlike the earthquake signal with highly similar waveforms and coherent time-frequency patterns over all stations, the rockfall signals of all stations are highly variable in the time and frequency domains. High-frequency (larger than 10 Hz) energy dominates rockfall waveforms at near-field stations. The relative low-frequency energy dominates the far-field stations' rockfall recordings since the high-frequency portion attenuates significantly with dissemination distances. We identify the engineering signals according to our experiences during fieldwork and determine the car-induced signals by inspecting the order and the speed of signal appearances across the stations. For the earthquake waveform recorded in situ, we detected and manually checked the P and S arrivals using the RED-PAN model [22]. Finally, we identified 348 rockfall events recorded by more than two stations with 750 sets of waveforms; 1,399 sets of rockfall waveforms labeled with only one station; 193 car-induced events with 495 sets of waveforms; 280 sets of engineering signals with 455 waveforms; and 1,834 earthquake events with 5,324 waveforms. The Luhu dataset is partitioned into the training and testing sets in a 70%-30% ratio. All the potential rockfall waveforms labeled with only one station are not included in the test set.

B. Additional training dataset and data augmentation

The lack of sufficient samples has always been problematic when training rockfall detection algorithms. This study includes hundreds of thousands of earthquake and nonearthquake samples for model training. Under the multitask learning framework, the additional large dataset of nonrockfall samples can facilitate the model's interpretation capability on seismograms and help develop a rockfall waveforms pattern recognition capability by sharing information among different tasks. The marching mosaic waveform augmentation (MMWA) and earthquake early warning augmentation (EEWA) approaches are applied to enhance the model's generalizability. The MMWA superimposes multiple earthquake samples on each other and shifts semisynthetic waveforms back and forth. The EEWA allows for time-clipped earthquake waveforms in which only P waves are visible under the receptive field of the model [22]. We collected and generated the earthquake and nonearthquake samples from the Taiwan earthquake dataset and the STEAD dataset for the single-station model. To develop the association model, the earthquake and nonearthquake samples were generated from the INSTANCE dataset, with each consisting of four station recordings with a random station order. Both models' training and validation data ratio are 80%-20%.

When addressing large additional earthquake training samples, imbalanced learning with severely skewed class distributions is another challenge to overcome; we apply the MMWA strategy to superimpose and randomly shift the rockfall and earthquake waveforms (Figure 2) to extend the datasets. The MMWA is applied to the training sets of both the single-station model and the association model, where we replicate the single-station mosaic waveforms four times as the inputs of the latter model. For the association model inputs of the four stations, we randomly set the station order of the input tensor to prevent the model from memorizing specific orders of recorded stations and waveforms. On the other hand, not all events have four station recordings among all the samples in the Luhu dataset; some might be missing data, or the target waveforms may not be sufficiently distinct for labeling. We complement or substitute these samples with random values for the association model.

III. Methods

Considering the data scarcity of rockfall events, we frame the rockfall detection task under multitask learning and transfer learning schema. Multitask learning enables knowledge transfer among different tasks and helps develop the task of learning with insufficient training data. Moreover, a multitask model is

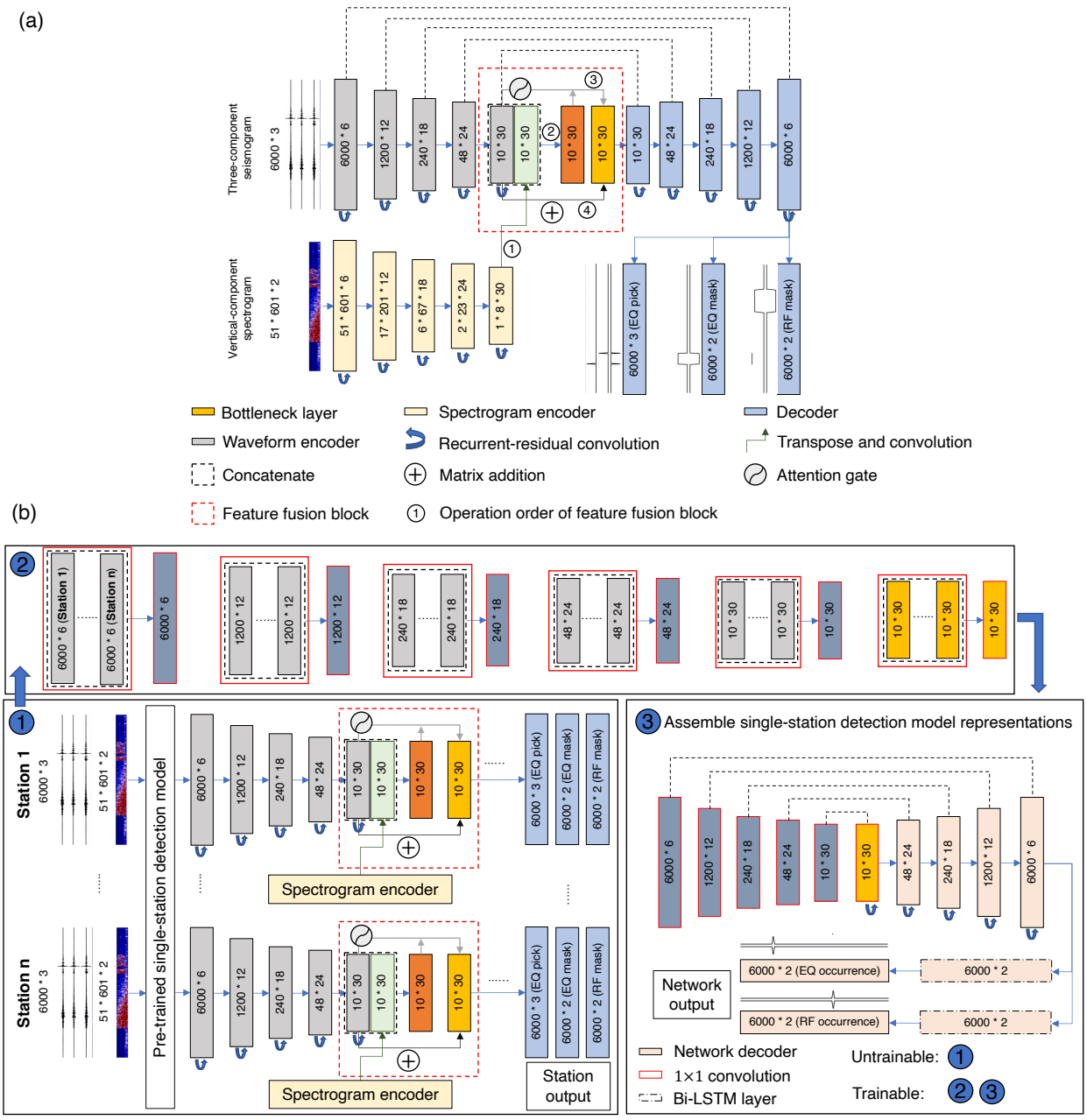

Fig. 3. Model architecture. (a) Three-component seismograms and vertical-component spectrograms are the inputs of the waveform encoder and the spectrogram encoder of the single-station detection model, respectively. The bottleneck layer is where the waveform encoder and the spectrogram encoder fuse, which also connects the model decoder and the waveform encoder. The outputs are the earthquake phase-time functions, the earthquake waveform masking functions, and the rockfall waveform masking functions. (b) The association model concatenates and merges the waveform encoder tensors of all station recordings, which are produced by the trained single-station detection model. The merged encoder is then skip-connected to the new trainable decoder to produce network outputs, the local occurrence time functions of earthquake and rockfall events.

more advantageous in terms of computational efficiency than deploying multiple models for various tasks. Transfer learning focuses on applying knowledge gained from pretrained tasks to other related but different problems. The association of rockfall events relies on assembling the a priori cognition of single-station waveforms. Transfer learning is applied here to inherit and assemble single-station detection model representations of all station recordings for event identification.

A. Single-station detection model

An earthquake signal typically includes P and S phases and is prone to waveform pattern recognition. In comparison, rockfall signals are induced by rock impacts with various sizes on the weight-bearing medium with rolling, free-falling, or bouncing movements. Thus, a rockfall waveform can appear as successive or discrete pulse-like signals with broad energy frequency ranges and is usually more easily identified in the time-frequency domain. We take the waveforms and spectrogram as the inputs of the single-station detection model based on our

experiences, which provides more confidence when confirming a target signal (Figure 3 (a)). Note that the spectrogram is obtained by using a short-time Fourier transform with a 0.2-second Hanning window and a 50% overlap rate.

The single-station detection model consists of a waveform encoder, a spectrogram encoder, a feature fusion block, and a decoder (Figure 3 (a)). The two encoders separately map the Z score standardized input data (i.e., three-component waveforms for the waveform encoder and the vertical-component spectrogram for the spectrogram encoder) to a high-dimensional feature space with a series of recurrent-residual convolution blocks [22]–[24]. The subsequent feature fusion block merges the two encoder features as the input of the decoder, which is also composed of a series of recurrent-residual convolution blocks and is skip-connected with the waveform encoder. Let α be outputs of the last layer of the waveform encoder. We apply an additional convolution operation to the outputs of the last layer of the spectrogram encoder to match the shape of α, where the resulting output is denoted as β. The feature fusion block first merges α and β with a convolution operation via concatenation: $\gamma = conv([\alpha; \beta])$, where AG denotes an attention gate [24], and the feature fusion block output ν is defined as $\nu = AG(target : \gamma; gate : \alpha) + \alpha$. The decoder finally outputs three sets of vectors associated with the assigned tasks of earthquake phase arrival time picking, earthquake waveform masking, and rockfall waveform masking.

B. Association model

The encoders of the single-station detection model learn to extract informative features from the input data to accomplish the assigned tasks. The core idea of the association model is to assemble the encoder representations of the single-station detection model for all station recordings and determine the seismic event occurrence times, which are highly related to the tasks of the single-station model. Let τ_i^n be the encoder outputs of the single-station detection model at a depth of n with the data of input station i. We perform a 1x1 convolution on the concatenation of τ^n (i.e., $[\tau_1^n; \tau_2^n; \tau_3^n; \tau_4^n]$ in this study) to form the association model encoder at various depths (Figure 3 (b)). The encoder is then skip-connected to a series of recurrent-residual convolution blocks to produce the local network outputs, i.e., the occurrence time functions of earthquake and rockfall events. During the training process, we freeze the trained weights of the single-station detection model. In this way, the transfer of knowledge from the single-station detection model can help develop the association model without causing it to collapse.

Generally, the single-station detection model is independent but included in the association model, and the prediction results of the two models do not interfere with each other. Rather than training a single model that can produce the same outputs, we build RockNet with two related but independent models. The reason for this is that many more computing resources are needed to train a new model that optimizes both the single-station detection and association tasks from scratch. Additionally, it is difficult to apply data augmentation methods such as MMWA and EEWA [22] to network-based data, where the waveform amplitude and the source-receiver distance should be considered.

C. Target function prototypes and model optimization

RockNet optimizes two types of target functions: mask functions that wrap the target waveforms and truncated Gaussian functions that are transformed from the ground-truth time labels of the P and S phase arrivals of earthquakes and seismic event occurrences with standard deviations of 0.2, 0.3 and 0.5 seconds. Overall, the two models of RockNet are built under a multitask learning framework. The single-station model optimizes three tasks: seismic phase arrival time picking, earthquake waveform masking, and rockfall waveform masking (Figure 3 (a)). The association model optimizes two functions for estimating the local occurrences of earthquake and rockfall events, in which the truncated Gaussian functions are centered at the sample 0.5 seconds before the first label of all stations (Figure 3 (b)). For every task, we add an "others" class to meet the softmax normalization criterion of the model output layer, which squeezes the model outputs to [0, 1] and sums them up to 1 for every sample along the time axis. During model training, cross-entropy is applied as a loss function $\mathbf{H}$ to estimate the differences between the current predictions $\mathbf{p}$ (i.e., the softmax-normalized outputs) and the target functions $\mathbf{q}$ for model optimization purposes; the optimizer is Adam [25] with a learning rate of 1e-4 in this study:

$$\mathbf{H}(\mathbf{p}, \mathbf{q}) = -\sum_{x}^{6000} \sum_{1}^{N} \mathbf{p}_N(x) \log \mathbf{q}_N(x) \tag{1}$$

In equation 1, x refers to the number of samples along the time axis (a total of 6,000 samples in this study), and N refers to the number of target function vectors (3 for the earthquake phase arrival time picking functions and 2 for the other functions). The total loss L of training epoch I is defined as the weighted sum of the cross-entropy values computed for each task $\mathbf{k}$:

$$L(I) = \sum_{\mathbf{k}}^{N} \lambda_{\mathbf{k}}(I) \mathbf{H}(\mathbf{p}(I), \mathbf{q}(I))_{\mathbf{k}} \tag{2}$$

where the task weightings λ are estimated using the dynamic weight averaging (DWA) strategy [22], [26].

IV. Results

A. Benchmark test on the Luhu dataset

Table I lists the detection performance achieved by RockNet on the Luhu dataset, with 0.5 set as the positive detection threshold. For instance, a rockfall sample detected with a mean rockfall mask value that is larger than 0.5 is a true-positive prediction for the rockfall class of the single-station detection model. A rockfall event sample detected with a peak rockfall occurrence value that is larger than 0.5 is a true-positive prediction for the association model. Considering the single-station detection model, we compare the performances achieved by the model with and without the vertical-component spectrogram serving as the model input. With the additional time-frequency information, the model improves its rockfall

TABLE I
MODEL PERFORMANCE ACHIEVED ON THE LUHU TESTING DATASET [a].

-	Single-station detection model						Association model					
Description	Compare the effect of input data						Compare the effect of training size					
Model	Waveform + Vertical-component spectrogram			Waveform			Luhu dataset + INSTANCE			Luhu dataset		
Training size	393K			393K			440K			47K		
Class	EQ	RF	Nz	EQ	RF	Nz	EQ	RF	Nz	EQ	RF	Nz
Test size	1581	218	980	1581	218	980	551	100	346	551	100	346
Precision	0.990	0.981	0.991	0.989	0.995	0.967	0.993	1.000	0.986	0.996	0.986	0.920
Recall	1.000	0.959	0.980	0.999	0.853	0.982	1.000	0.930	0.994	0.998	0.710	0.991
F1-score	0.995	0.970	0.985	0.994	0.919	0.974	0.996	0.964	0.990	0.997	0.826	0.954
Macro F1-score		0.983			0.962			0.983			0.926	

[a]EQ, RF, and Nz refer to earthquakes, rockfalls, and local noise, respectively.

recall rate by 10.6%, indicating fewer false-negative detections (i.e., misidentifying rockfalls as earthquakes and noise). For the association model, we explore the training data quantity factor under the transfer learning framework. The association model that trains with only the Luhu dataset achieves a macro F1 score of 0.926 under the transfer learning framework. With the additional training dataset of INSTANCE, we obtain a macro F1 score of 0.983, in which the rockfall recall rate improves by 22%, and the precision rate of local noise improves by 6.6%. Figure 4 shows prediction examples in which the rockfall waveform amplitude, signal-to-noise ratio (SNR), and high-frequency energy attenuate with increasing distance.

B. Examination on the Super-Sauze unstable slope dataset

We also examined the generalization of our trained model using an independent dataset collected at the Super-Sauze unstable slope [14], which includes labeled events of anthropogenic/environmental noises (351 events), earthquakes (355 events with SNR >2), rockfalls (357 events with SNR>2). The labeled dataset was acquired from three time periods: from 11 October to 19 November 2013, from 10 to 30 November 2014, and from 9 June to 15 August 2015; and recorded by six one-component short-period-seismometers (Noemax and Sercel L4C) and two three-component broadband-seismometers (RefTek 130S-01). The eight seismometers are arranged as two equilateral triangular arrays that a three-component seismometers placed at center surrounded by three vertical one-component seismometers, installed at the east and west sides of the Super-Sauze unstable slope. To formulate the input of four three-component seismograms for our model, we treat the three vertical one-component seismograms as a three-channel vector and thus meet the input criterion. The association model achieves a macro F1 score of 0.940, with F1 scores of 0.916, 0.973, and 0.930 for noises, earthquakes, and rockfalls, respectively (table II).

V. DISCUSSIONS

In this study, we identify rockfall events by emulating the decision-making process of human experts. That is, we characterize potential rockfall waveforms based on both time series data and the time-frequency representations of each station and confirm an event according to the waveform appearances and energy decay statuses of other stations. For

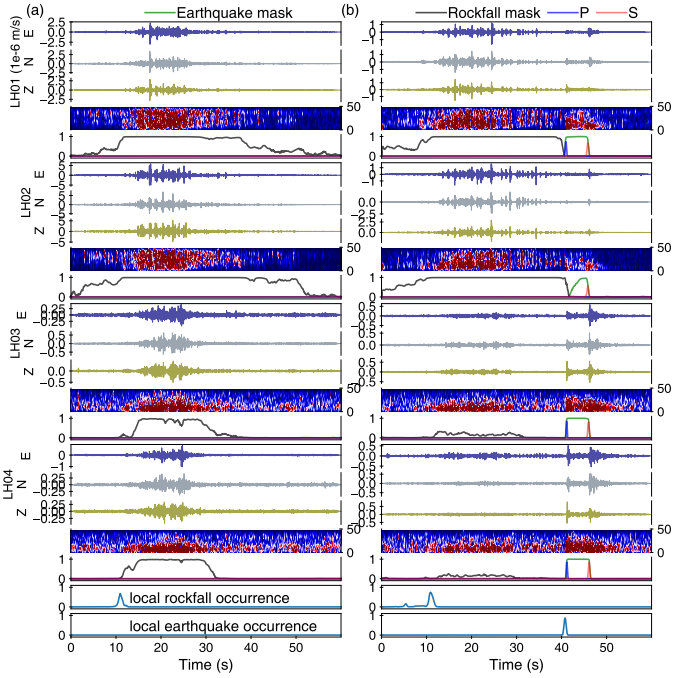

Fig. 4. Detection examples of rockfall events that occur between stations LH01 and LH02. These examples are not included in the training data. (a)(b) The overall rockfall waveform amplitudes, SNRs, and high-frequency energy attenuation processes from stations LH01 and LH02 to stations LH03 and LH04 are conspicuous. (b) The P wave of the earthquake strongly interferes with the rockfall waveform, and the single-station model does not detect the arrival of the phase at station LH02. The rockfall waveform amplitude and SNR discrepancies are more evident than the earthquake waveforms with same-scale amplitudes over all stations. Nevertheless, the association model still identifies the earthquake and rockfall occurrences with high prediction values.

TABLE II
ASSOCIATION MODEL PERFORMANCE ON THE SUPER-SAUZE DATASET.

Class	EQ	RF	Nz
Test size	355	357	351
Precision	0.967	0.950	0.903
Recall	0.980	0.910	0.929
F1-score	0.973	0.930	0.916
Macro F1-score		0.940	

example, in Figure 4(b), the rockfall waveform is unclear at stations LH03 and LH04, and the P wave of the earthquake interferes with the rockfall waveform. Other station recordings can confirm the coherency of the rockfall and earthquake occurrences. In the experiments comparing different inputs for the single-station detection model (table I), we achieve substantial improvements in the rockfall recall rate. The performance improvement conforms to our experiences in distinguishing between different seismic sources, in which time-frequency representations help when time series features are not highly typical. On the other hand, the association model benefits from training with the additional INSTANCE dataset, which makes the total dataset more imbalanced. However, the association model performs better (table I), and we infer that its advances are derived from the positive transfer of knowledge from the well-trained single-station detection model. The test results of the independent Super-Sauze dataset show that our trained model generalizes well. This may be because the physical mechanisms behind the events in different regions are similar, as reflected in the seismic recordings [27]. Therefore, the trained model has the potential to be used in other areas for rockfall and earthquake monitoring.

VI. Conclusions

We develop a deep learning-based rockfall and earthquake detection model for a local seismic network, RockNet, which performs joint detection with each station and determines the local occurrences of seismic events by associating the model responses of all station recordings. We address the imbalanced learning problem by adopting multitask learning and transfer learning strategies and by utilizing a data augmentation technique that superimposes and shifts rockfall and earthquake waveforms. RockNet exhibits the potential to perform onsite rockfall seismic monitoring. Additionally, RockNet can serve as a template for training a deep learning model to detect the seismic sources of insufficient training data, such as landslides and volcanic signals.

VII. Open Research

The labeled data [28] are available in Dryad (https://doi.org/10.5061/dryad.tx95x6b2f). The code and model are open source at GitHub (https://github.com/tso1257771/RockNet) and Zenodo (https://doi.org/10.5281/zenodo.7458571, [29]).

Acknowledgment

This work was jointly supported by the National Science and Technology Council (NSTC), R.O.C. (110-2116-M-006-011, 111-2116-M-006 -017, and 109-2116-M-006-018), the Soil and Water Conservation Bureau, Taiwan (SWCB-108-294 and SWCB-109-227), the Nielson Energy Fellowship provided by the School of Energy Resources, University of Wyoming, a fellowship of MOST supporting Wu-Yu Liao's Ph.D. study, a fellowship of the French Agence Nationale de la Recherche (ANR-20-CE01-0006, project HighLand) supporting F. Provost's Post-Doc, and the National Center for High-performance Computing (NCHC), Taiwan for providing some computational and storage resources. The continuous seismic data of the Luhu unstable slope were provided by the National Science and Technology Center for Disaster Reduction, Taiwan. The continuous seismic data of the Super-Sauze unstable slope were provided by the Observatoire Multi-disciplinaire des Instabilités de Versant [30].

References

[1] M. Krautblatter and M. Moser, "A nonlinear model coupling rockfall and rainfall intensity based on a four year measurement in a high alpine rock wall (reintal, german alps)," *Natural Hazards and Earth System Sciences*, vol. 9, no. 4, pp. 1425–1432, 2009. [Online]. Available: https://nhess.copernicus.org/articles/9/1425/2009/

[2] A. Helmstetter and S. Garambois, "Seismic monitoring of séchilienne rockslide (french alps): Analysis of seismic signals and their correlation with rainfalls," *Journal of Geophysical Research*, vol. 115, no. F3, Aug. 2010. [Online]. Available: https://doi.org/10.1029/2009jf001532

[3] A. Delonca, Y. Gunzburger, and T. Verdel, "Statistical correlation between meteorological and rockfall databases," *Natural Hazards and Earth System Sciences*, vol. 14, no. 8, pp. 1953–1964, 2014. [Online]. Available: https://nhess.copernicus.org/articles/14/1953/2014/

[4] J. D'Amato, D. Hantz, A. Guerin, M. Jaboyedoff, L. Baillet, and A. Mariscal, "Influence of meteorological factors on rockfall occurrence in a middle mountain limestone cliff," *Natural Hazards and Earth System Sciences*, vol. 16, no. 3, pp. 719–735, 2016. [Online]. Available: https://nhess.copernicus.org/articles/16/719/2016/

[5] M. Lato, J. Hutchinson, M. Diederichs, D. Ball, and R. Harrap, "Engineering monitoring of rockfall hazards along transportation corridors: using mobile terrestrial lidar," *Natural Hazards and Earth System Sciences*, vol. 9, no. 3, pp. 935–946, 2009. [Online]. Available: https://nhess.copernicus.org/articles/9/935/2009/

[6] H. Lan, C. D. Martin, C. Zhou, and C. H. Lim, "Rockfall hazard analysis using lidar and spatial modeling," *Geomorphology*, vol. 118, no. 1, pp. 213–223, 2010. [Online]. Available: https://www.sciencedirect.com/science/article/pii/S0169555X10000127

[7] M. J. Lato, M. S. Diederichs, D. J. Hutchinson, and R. Harrap, "Evaluating roadside rockmasses for rockfall hazards using LiDAR data: optimizing data collection and processing protocols," *Natural Hazards*, vol. 60, no. 3, pp. 831–864, Jun. 2011. [Online]. Available: https://doi.org/10.1007/s11069-011-9872-y

[8] M. J. Royán, A. Abellán, M. Jaboyedoff, J. M. Vilaplana, and J. Calvet, "Spatio-temporal analysis of rockfall pre-failure deformation using terrestrial LiDAR," *Landslides*, vol. 11, no. 4, pp. 697–709, Nov. 2013. [Online]. Available: https://doi.org/10.1007/s10346-013-0442-0

[9] A. M. Fanos, B. Pradhan, S. Mansor, Z. M. Yusoff, and A. F. bin Abdullah, "A hybrid model using machine learning methods and GIS for potential rockfall source identification from airborne laser scanning data," *Landslides*, no. 9, pp. 1833–1850, Apr. 2018. [Online]. Available: https://doi.org/10.1007/s10346-018-0990-4

[10] N. Matsuoka, "A multi-method monitoring of timing, magnitude and origin of rockfall activity in the japanese alps," *Geomorphology*, vol. 336, pp. 65–76, 2019. [Online]. Available: https://www.sciencedirect.com/science/article/pii/S0169555X19301230

[11] C. Hibert, A. Mangeney, G. Grandjean, and N. M. Shapiro, "Slope instabilities in dolomieu crater, réunion island: From seismic signals to rockfall characteristics," *Journal of Geophysical Research: Earth Surface*, vol. 116, no. F4, 2011. [Online]. Available: https://agupubs.onlinelibrary.wiley.com/doi/abs/10.1029/2011JF002038

[12] F. Dammeier, J. R. Moore, F. Haslinger, and S. Loew, "Characterization of alpine rockslides using statistical analysis of seismic signals," *Journal of Geophysical Research*, vol. 116, no. F4, Nov. 2011. [Online]. Available: https://doi.org/10.1029/2011jf002037

[13] V. L. Zimmer and N. Sitar, "Detection and location of rock falls using seismic and infrasound sensors," *Engineering Geology*, vol. 193, pp. 49–60, 2015. [Online]. Available: https://www.sciencedirect.com/science/article/pii/S0013795215001234

[14] F. Provost, C. Hibert, and J.-P. Malet, "Automatic classification of endogenous landslide seismicity using the random forest supervised classifier," *Geophysical Research Letters*, vol. 44, no. 1, pp. 113–120, 2017. [Online]. Available: https://doi.org/10.1002/2016gl070709

[15] C. Hibert, F. Provost, J.-P. Malet, A. Maggi, A. Stumpf, and V. Ferrazzini, "Automatic identification of rockfalls and volcano-tectonic earthquakes at the piton de la fournaise volcano using a random forest algorithm," *Journal of Volcanology and Geothermal Research*, vol. 340, pp. 130–142, jun 2017. [Online]. Available: https://doi.org/10.1016%2Fj.jvolgeores.2017.04.015

[16] P. Bottelin, D. Jongmans, D. Daudon, A. Mathy, A. Helmstetter, V. Bonilla-Sierra, H. Cadet, D. Amitrano, V. Richefeu, L. Lorier, L. Baillet, P. Villard, and F. Donzé, "Seismic and mechanical studies of the artificially triggered rockfall at mount néron (french alps, december 2011)," *Natural Hazards and Earth System Sciences*, vol. 14, no. 12, pp. 3175–3193, dec 2014. [Online]. Available: https://doi.org/10.5194%2Fnhess-14-3175-2014

[17] L. Feng, V. Pazzi, E. Intrieri, T. Gracchi, and G. Gigli, "Rockfall seismic features analysis based on in situ tests: frequency, amplitude, and duration," *Journal of Mountain Science*, vol. 16, no. 5, pp. 955–970, may 2019. [Online]. Available: https://doi.org/10.1007%2Fs11629-018-5286-6

[18] C. Hibert, F. Noël, D. Toe, M. Talib, M. Desrues, E. Wyser, O. Brenguier, F. Bourrier, R. Toussaint, J.-P. Malet, and M. Jaboyedoff, "Machine learning prediction of the mass and the velocity of controlled single-block rockfalls from the seismic waves they generate," *EGUsphere*, vol. 2022, pp. 1–25, 2022. [Online]. Available: https://egusphere.copernicus.org/preprints/egusphere-2022-522/

[19] S. M. Mousavi, Y. Sheng, W. Zhu, and G. C. Beroza, "STanford EArthquake dataset (STEAD): A global data set of seismic signals for AI," *IEEE Access*, vol. 7, pp. 179 464–179 476, 2019, conference Name: IEEE Access.

[20] A. Michelini, S. Cianetti, S. Gaviano, C. Giunchi, D. Jozinović, and V. Lauciani, "Instance the italian seismic dataset for machine learning," 2021. [Online]. Available: http://www.pi.ingv.it/instance/

[21] R. Allen, "Automatic phase pickers: Their present use and future prospects," *Bulletin of the Seismological Society of America*, vol. 72, no. 6B, pp. S225–S242, 1982.

[22] W. Liao, E.-J. Lee, D. Chen, P. Chen, D. Mu, and Y.-M. Wu, "RED-PAN: Real-Time Earthquake Detection and Phase-Picking With Multitask Attention Network," *IEEE Transactions on Geoscience and Remote Sensing*, vol. 60, pp. 1–11, 2022.

[23] M. Z. Alom, M. Hasan, C. Yakopcic, T. M. Taha, and V. K. Asari, "Recurrent residual convolutional neural network based on u-net (r2u-net) for medical image segmentation," *arXiv preprint arXiv:1802.06955*, 2018.

[24] W. Liao, E.-J. Lee, D. Mu, P. Chen, and R.-J. Rau, "ARRU Phase Picker: Attention Recurrent-Residual U-Net for Picking Seismic P- and S-Phase Arrivals," *Seismological Research Letters*, vol. 92, no. 4, pp. 2410–2428, 03 2021. [Online]. Available: https://doi.org/10.1785/0220200382

[25] D. P. Kingma and J. Ba, "Adam: A method for stochastic optimization," 2014. [Online]. Available: https://arxiv.org/abs/1412.6980

[26] S. Liu, E. Johns, and A. J. Davison, "End-to-end multi-task learning with attention," *Proceedings of the IEEE Conference on Computer Vision and Pattern Recognition*, pp. 1871–1880, 2019.

[27] F. Provost, J.-P. Malet, C. Hibert, A. Helmstetter, M. Radiguet, D. Amitrano, N. Langet, E. Larose, C. Abancó, M. Hürlimann, T. Lebourg, C. Levy, G. Le Roy, P. Ulrich, M. Vidal, and B. Vial, "Towards a standard typology of endogenous landslide seismic sources," *Earth Surface Dynamics*, vol. 6, no. 4, pp. 1059–1088, 2018. [Online]. Available: https://esurf.copernicus.org/articles/6/1059/2018/

[28] W. Liao, E.-J. Lee, C.-C. Wang, and P. Chen, "Data from: Rocknet: Rockfall and earthquake detection and association via multitask learning and transfer learning,," 2023.

[29] W. Liao, "Rocknet: Rockfall and earthquake detection and association via multitask learning and transfer learning," Dec. 2022. [Online]. Available: https://doi.org/10.5281/zenodo.7458571

[30] Observatoire Multidisciplinaire Des Instabilités De Versant, "Omiv - time serie of seismic waveforms recorded on landslides and catalogue of endogenous seismic events," 2012. [Online]. Available: https://dataosu.obs-besancon.fr/FR-18008901306731-2018-12-03-02_OMIV-Time-serie-of-seismic-waveforms-recorded.html